Available online at www.sciencedirect.com

SCIENCE DIRECT®

Journal of Computational Physics 195 (2004) 153–174

JOURNAL OF COMPUTATIONAL PHYSICS

www.elsevier.com/locate/jcp

Adaptive finite elements with high aspect ratio for the computation of coalescence using a phase-field model

E. Burman [a,1], A. Jacot [b,c], M. Picasso [a,*]

[a] *Departement de Mathematiques, Faculté des Sciences de Base, Ecole Polytechnique Fédérale de Lausanne, Institut d'Analyse et Calcul Scientifique, Lausanne CH 1015, Switzerland*

[b] *Laboratoire de Métallurgie Physique, Faculté des Sciences et Techniques de l'Ingénieur, Ecole Polytechnique Fédérale de Lausanne, Institut des Matériaux, Lausanne 1015, Switzerland*

[c] *Calcom SA, Parc Scientifique, Lausanne 1015, Switzerland*

Received 7 January 2003; received in revised form 11 July 2003; accepted 20 September 2003

Abstract

A multiphase-field model for the description of coalescence in a binary alloy is solved numerically using adaptive finite elements with high aspect ratio. The unknown of the multiphase-field model are the three phase fields (solid phase 1, solid phase 2, and liquid phase), a Lagrange multiplier and the concentration field. An Euler implicit scheme is used for time discretization, together with continuous, piecewise linear finite elements. At each time step, a linear system corresponding to the three phases plus the Lagrange multiplier has to be solved. Then, the linear system pertaining to concentration is solved. An adaptive finite element algorithm is proposed. In order to reduce the number of mesh vertices, the generated meshes contain elements with high aspect ratio. The refinement and coarsening criteria are based on an error indicator which has already been justified theoretically for simpler problems. Numerical results on two test cases show the efficiency of the method.

1. Introduction

Over the last decade, considerable progress has been made in numerical simulation of solidification microstructures [1]. Although sharp interface models are still in development for the description of dendritic growth (see, for instance [2,3] for recent works), the phase-field has emerged as a method of choice, namely due to the advantage of avoiding the difficult problem of tracking sharp interfaces in two or three space dimensions. The principles of the phase-field model have been described in detail in numerous publications [4–17] (see [14,15] for recent reviews and [4–7,16,17] for some of the mathematical aspects). The idea is to describe the location of the solid and liquid phases in the computational

---

[*] Corresponding author. Tel.: +41-216-9342-97; fax: +41-216-9343-03.
E-mail address: marco.picasso@epfl.ch (M. Picasso).

[1] Supported by the Swiss National Science Foundation.

0021-9991/$ - see front matter © 2003 Elsevier Inc. All rights reserved.
doi:10.1016/j.jcp.2003.09.021

domain by introducing an order parameter – the phase field – which varies smoothly from one to zero (sometimes from −1 to +1) through a diffuse interface. Partial differential equations describing the evolution of the phase and temperature fields (or concentration for thermodynamic systems with more than one component) are obtained by minimizing a Gibbs free energy function. The phase-field concept has been extended to deal with problems involving more than two phases thus introducing multiple order parameters, for instance in eutectic or peritectic reactions [18–20]. The so-called multiphase-field approach was also used to study the coalescence between dendrite arms and solid regions belonging to different grains in a binary alloy [21].

All of the phase-field models are very challenging from the numerical point of view. The main difficulty is due to the very rapid change of the phase field (and also the concentration field in alloys) across the diffuse interface, whose thickness has to be taken very small to correctly capture the physics of the phase transformation. Since we are interested in coalescence of binary alloys, the width of the diffuse interface should be between 1 and 10 nm. A high spatial resolution is, therefore, needed to describe the smooth transition, and consequently explicit methods formulated on regular grids require very large numbers of grid points and time steps. In order to reduce the computational time and the memory requirements, adaptive finite elements have been developed [22,23], using isotropic finite elements. Recently, a phase-field model based on adaptive finite elements with high aspect ratio and an implicit formulation of diffusion terms was proposed in order to further reduce the number of vertices and time steps required for a computation [24]. The model uses refinement and coarsening criteria based on an error indicator which was justified theoretically for simpler problems in [25,26].

The goal of this paper is to use adaptive finite elements with high aspect ratio to perform multiphase-field computations with the model of Rappaz et al. [21]. This paper contains three original contributions. First, the model of Rappaz et al. [21] is extended to include the anisotropy of surface energy. We found it more convenient to write the model in weak form, this being also more suitable to the use of finite elements. Second, in order to avoid numerical instabilities due to the constraint between the phases (the sum of all the phase fields must be one), we have adopted an implicit formulation that couples all the unknowns at each time step. We prove that the obtained linear system is invertible, this being the first step towards well-posedness of the model. Third, adaptive finite elements with high aspect ratio are used in order to reduce the number of mesh vertices, therefore, a suitable error indicator must be introduced to define the refinement and coarsening criteria. For details about the adaptive procedure, we refer to papers published elsewhere for simpler problems [24–26]. The use of adaptive finite elements with high aspect ratio is of great interest for coalescence problems, due to the fact that a realistic value of interface thickness (about 1 nm) has to be taken for a quantitative description of the problem. (If coalescence is not the issue, computations of dendritic growth can generally be performed with a larger interface thickness without introducing a substantial deviation from the sharp interface problem.)

The outline of the paper is the following. In the following section, the model of Rappaz et al. [21] is presented and extended to introduce the anisotropy of the surface energy. The corresponding weak formulation is proposed in Section 3 and the numerical method in Section 4. Section 5 is devoted to the adaptive finite element algorithm and the refinement and coarsening criteria. In Section 6, numerical results for two test cases are presented to illustrate the efficiency of the method. Finally, the proof that the linear system obtained in Section 4 is invertible is proposed in Appendix A.

2. The model

The model is based on the multiphase-field approach developed in [21] to describe solidification and coalescence of several grains in a binary alloy. The unknowns are two solid phase fields ϕ_1 and ϕ_2 corresponding to two grains, the liquid phase field ϕ_3, the Lagrange multiplier corresponding to the constraint

$$\phi_1 + \phi_2 + \phi_3 = 1, \tag{1}$$

and the concentration field c (for instance, the concentration of carbon into iron), see Fig. 1.

Following [21], a free energy functional is formulated in the computational domain Ω. It can be written as the sum of the Gibbs free energy associated with phase transformations plus double well barriers and an interfacial energy contribution. The anisotropic interfacial energy contribution J_{int} can be written as:

$$J_{\text{int}}(\phi_1,\phi_2,\phi_3) = \frac{\epsilon_{12}^2}{2}\int_\Omega a^2(\theta_{12}(\mathbf{r}(\phi_1,\phi_2)))|\mathbf{r}(\phi_1,\phi_2)|^2 + \frac{\epsilon_{13}^2}{2}\int_\Omega a^2(\theta_{13}(\mathbf{r}(\phi_1,\phi_3)))|\mathbf{r}(\phi_1,\phi_3)|^2 + \frac{\epsilon_{23}^2}{2}\int_\Omega a^2(\theta_{23}(\mathbf{r}(\phi_2,\phi_3)))|\mathbf{r}(\phi_2,\phi_3)|^2.$$

Here, ϵ_{12}, ϵ_{13}, and ϵ_{23} are positive parameters,

$$\mathbf{r}(\phi_i,\phi_j) = \phi_i\nabla\phi_j - \phi_j\nabla\phi_i \quad (i,j) \in \{(1,2),(1,3),(2,3)\},$$

a is the real valued function defined as in [13] by

$$a(\theta) = 1 + \bar{a}\cos(\kappa\theta) \quad \forall\theta \in \mathbb{R}, \tag{2}$$

$\bar{a}$ is the anisotropy coefficient and κ the symmetry order of the crystal (that is the number of primary dendrite arms). Finally θ_{ij}, $(i,j) \in \{(1,2),(1,3),(2,3)\}$, is defined for all $\boldsymbol{\xi} = (\xi_1,\xi_2)^{\mathrm{T}} \in \mathbb{R}^2$ by

$$\cos\left(\theta_{ij}(\boldsymbol{\xi}) + \theta_{ij}^0\right) = \frac{\xi_1}{\sqrt{(\xi_1)^2 + (\xi_2)^2}}, \tag{3}$$

where θ_{ij}^0 are given parameters. For instance, θ_{13}^0 (resp., θ_{23}^0) corresponds to the anisotropy growth angle of a dendrite made out of phase 1 (resp., phase 2) into the liquid, see Fig. 2. The Gibbs free energy associated with phase transformation J_{tr} can be written as

$$J_{\text{tr}}(\phi_1,\phi_2,\phi_3) = \int_\Omega \frac{L}{T_{\text{m}}} m_{\text{l}}\left(\frac{c}{\phi_3 + k(1-\phi_3)} - \frac{T - T_{\text{m}}}{m_{\text{l}}}\right)\phi_3^3(10 - 15\phi_3 + 6\phi_3^2).$$

Here, L is the volumetric latent heat, T_{m} the melting temperature of the pure material (i.e., when the concentration is zero), T the current temperature (homogeneous in the whole computational domain Ω), m_{l}

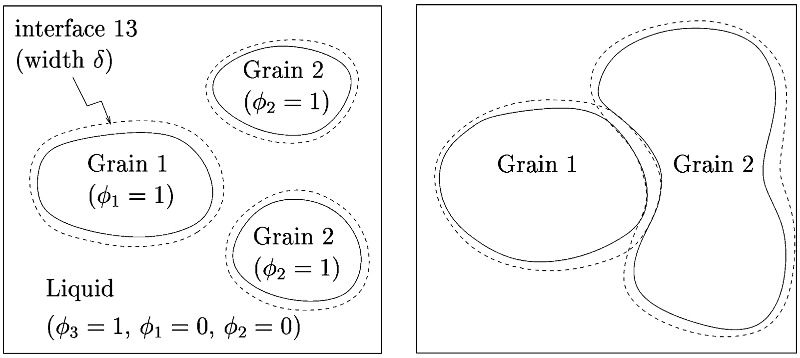

Fig. 1. Solidification of a binary alloy using the multiphase-field model. Grains 1 and 2 are solid phases. Phase 3 is the liquid phase. At initial time three solid regions are present in the computational domain (left). Two of them correspond to the same grain (for instance, two arms of the same three-dimensional dendrite). After some time, the two regions belonging to the same grain have coalesced, whereas the two grains are still separated by a liquid film.

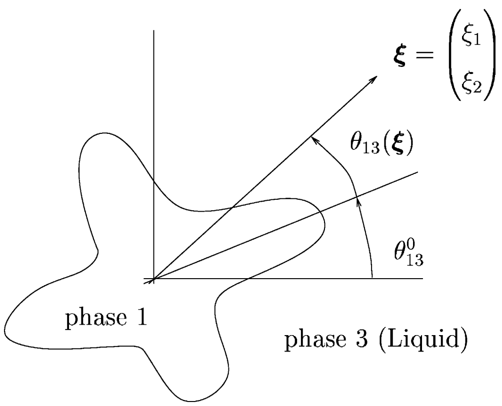

Fig. 2. Example of anisotropy of surface energy between phases 1 and 3. The angle θ_{13}^0 corresponds to the orientation of the crystal with respect to the reference axis.

the slope of the liquidus line, and k the partition coefficient in the phase diagram. Finally, the contribution of the double well potentials J_{dw} can be written as

$$J_{\mathrm{dw}}(\phi_1, \phi_2, \phi_3) = \int_\Omega W_{12}\phi_1^2\phi_2^2 + W_{13}\phi_1^2\phi_3^2 + W_{23}\phi_2^2\phi_3^2,$$

where W_{12}, W_{13}, and W_{23} are positive parameters.

Let us introduce the Lagrangian

$$\mathscr{L}(\phi_1, \phi_2, \phi_3, \lambda) = (J_{\mathrm{int}} + J_{\mathrm{tr}} + J_{\mathrm{dw}})(\phi_1, \phi_2, \phi_3) + \int_\Omega \lambda(\phi_1 + \phi_2 + \phi_3 - 1).$$

The set of functions ϕ_1, ϕ_2, ϕ_3 that minimize the functional $J_{\mathrm{int}} + J_{\mathrm{tr}} + J_{\mathrm{dw}}$ under the constraint (1) must satisfy $\mathscr{D}\mathscr{L}(\phi_1, \phi_2, \phi_3, \lambda) = 0$, where $\mathscr{D}$ denotes the formal Gateaux derivative. Then, given the kinetic coefficient M, the multiphase-field equations correspond to the following set of parabolic equations:

$$\begin{aligned}
&\frac{1}{M}\frac{\partial\phi_1}{\partial t} + \mathscr{D}_{\phi_1}\mathscr{L}(\phi_1, \phi_2, \phi_3, \lambda) = 0,\\
&\frac{1}{M}\frac{\partial\phi_2}{\partial t} + \mathscr{D}_{\phi_2}\mathscr{L}(\phi_1, \phi_2, \phi_3, \lambda) = 0,\\
&\frac{1}{M}\frac{\partial\phi_3}{\partial t} + \mathscr{D}_{\phi_3}\mathscr{L}(\phi_1, \phi_2, \phi_3, \lambda) = 0,\\
&\phi_1 + \phi_2 + \phi_3 - 1 = 0.
\end{aligned} \tag{4}$$

Following [20,21,27], this set of equations is supplemented with solute conservation

$$\frac{\partial c}{\partial t} = \operatorname{div}\left(D(\phi_3)\nabla c - \frac{D(\phi_3)(1-k)c}{\phi_3 + k(1-\phi_3)}\nabla\phi_3\right), \tag{5}$$

where $D(\phi_3) = D_{\mathrm{s}}(1-\phi_3) + D_{\mathrm{l}}\phi_3$, D_{s} and D_{l} being the solid and liquid diffusion coefficients, respectively.

3. Weak formulation

Let us consider the generic term of the interface energy J_{int} defined by

$$J(\phi_i,\phi_j)=\frac{\epsilon_{ij}^2}{2}\int_\Omega a^2(\theta_{ij}(\mathbf{r}(\phi_i,\phi_j)))|\mathbf{r}(\phi_i,\phi_j)|^2,$$

for $(i,j)\in\{(1,2);(1,3);(2,3)\}$. The formal Gateaux derivative in direction (ψ_i,ψ_j) is given by

$$\begin{aligned}\mathscr{D}J(\phi_i,\phi_j)(\psi_i,\psi_j)=\epsilon_{ij}^2&\int_\Omega a^2(\theta_{ij}(\mathbf{r}(\phi_i,\phi_j)))\mathbf{r}(\phi_i,\phi_j)\cdot\mathscr{D}\mathbf{r}(\phi_i,\phi_j)(\psi_i,\psi_j)\\&+\epsilon_{ij}^2\int_\Omega aa'(\theta_{ij}(\mathbf{r}(\phi_i,\phi_j)))\nabla\theta_{ij}(\mathbf{r}(\phi_i,\phi_j))\cdot\mathscr{D}\mathbf{r}(\phi_i,\phi_j)(\psi_i,\psi_j)|\mathbf{r}(\phi_i,\phi_j)|^2,\end{aligned}$$

where, using the definition of $\mathbf{r}$, we have

$$\mathscr{D}\mathbf{r}(\phi_i,\phi_j)(\psi_i,\psi_j)=\mathbf{r}(\phi_i,\psi_j)+\mathbf{r}(\psi_i,\phi_j),$$

and where, using (3), we have

$$|\boldsymbol{\xi}|^2\nabla\theta_{ij}(\boldsymbol{\xi})=|\boldsymbol{\xi}|^2\begin{pmatrix}\frac{\partial\theta_{ij}}{\partial\xi_i}(\xi_i,\xi_j)\\ \frac{\partial\theta_{ij}}{\partial\xi_j}(\xi_i,\xi_j)\end{pmatrix}=\begin{pmatrix}-\xi_j\\ \xi_i\end{pmatrix}.$$

Therefore, we obtain

$$\mathscr{D}J(\phi_i,\phi_j)(\psi_i,\psi_j)=\int_\Omega(B_{ij}(\phi_i,\phi_j)\mathbf{r}(\phi_i,\phi_j))\cdot(\mathbf{r}(\phi_i,\psi_j)+\mathbf{r}(\psi_i,\phi_j)),$$

the matrix B_{ij} being defined by

$$B_{ij}(\phi_i,\phi_j)=\epsilon_{ij}^2\begin{pmatrix}a^2(\theta_{ij}(\mathbf{r}(\phi_i,\phi_j))) & -aa'(\theta_{ij}(\mathbf{r}(\phi_i,\phi_j)))\\ aa'(\theta_{ij}(\mathbf{r}(\phi_i,\phi_j))) & a^2(\theta_{ij}(\mathbf{r}(\phi_i,\phi_j)))\end{pmatrix}.$$

Using again the definition of $\mathbf{r}$, we have

$$\begin{aligned}\mathscr{D}J(\phi_i,\phi_j)(\psi_i,\psi_j)=\int_\Omega\Big(&\phi_i^2(B_{ij}\nabla\phi_j)\cdot\nabla\psi_j-\phi_i\phi_j(B_{ij}\nabla\phi_i)\cdot\nabla\psi_j+\phi_j^2(B_{ij}\nabla\phi_i)\cdot\nabla\psi_i\\&-\phi_i\phi_j(B_{ij}\nabla\phi_j)\cdot\nabla\psi_i+\phi_i\psi_i(B_{ij}\nabla\phi_j)\cdot\nabla\phi_j-\phi_j\psi_i(B_{ij}\nabla\phi_i)\cdot\nabla\phi_j\\&+\phi_j\psi_j(B_{ij}\nabla\phi_i)\cdot\nabla\phi_i-\phi_i\psi_j(B_{ij}\nabla\phi_j)\cdot\nabla\phi_i\Big).\end{aligned}\qquad(6)$$

From the definition of the interfacial energy J_{int}, we have

$$\mathscr{D}J_{\mathrm{int}}(\phi_1,\phi_2,\phi_3)(\psi_1,\psi_2,\psi_3)=\sum_{(i,j)\in\{(1,2);(1,3);(2,3)\}}\mathscr{D}J(\phi_i,\phi_j)(\psi_i,\psi_j),$$

so that, using (6) we obtain the following condensed formulation:

$$\mathscr{D}J_{\mathrm{int}}(\vec{\phi},\vec{\psi})=(A(\vec{\phi},\nabla\vec{\phi})\nabla\vec{\phi},\nabla\vec{\psi})+(\tilde{A}(\vec{\phi},\nabla\vec{\phi})\vec{\phi},\vec{\psi}).$$

Here, $(\cdot,\cdot)$ stands for the $L^2(\Omega)$ scalar product, that is

$$(\vec{f},\vec{g}) = \int_\Omega \vec{f}\cdot\vec{g},$$

the vectors $\vec{\phi},\vec{\psi} \in \mathbb{R}^3$ and $\nabla\vec{\phi},\nabla\vec{\psi} \in \mathbb{R}^6$ are defined by

$$\vec{\phi} = \begin{pmatrix}\phi_1\\ \phi_2\\ \phi_3\end{pmatrix}, \quad \vec{\psi} = \begin{pmatrix}\psi_1\\ \psi_2\\ \psi_3\end{pmatrix}, \quad \nabla\vec{\phi} = \begin{pmatrix}\nabla\phi_1\\ \nabla\phi_2\\ \nabla\phi_3\end{pmatrix}, \quad \nabla\vec{\psi} = \begin{pmatrix}\nabla\psi_1\\ \nabla\psi_2\\ \nabla\psi_3\end{pmatrix},$$

and the matrices A and $\tilde{A}$ are defined by

$$A(\vec{\phi},\nabla\vec{\phi}) = \begin{pmatrix}\phi_2^2B_{12}+\phi_3^2B_{13} & -\phi_1\phi_2B_{12} & -\phi_1\phi_3B_{13}\\ -\phi_1\phi_2B_{12} & \phi_1^2B_{12}+\phi_3^2B_{23} & -\phi_2\phi_3B_{23}\\ -\phi_1\phi_3B_{13} & -\phi_2\phi_3B_{23} & \phi_1^2B_{13}+\phi_2^2B_{23}\end{pmatrix},$$

$$\tilde{A}(\vec{\phi},\nabla\vec{\phi}) = \begin{pmatrix}\tilde{A}_{11} & -(B_{12}\nabla\phi_1)\cdot\nabla\phi_2 & -(B_{13}\nabla\phi_1)\cdot\nabla\phi_3\\ -(B_{12}\nabla\phi_2)\cdot\nabla\phi_1 & \tilde{A}_{22} & -(B_{23}\nabla\phi_2)\cdot\nabla\phi_3\\ -(B_{13}\nabla\phi_3)\cdot\nabla\phi_1 & -(B_{23}\nabla\phi_3)\cdot\nabla\phi_2 & \tilde{A}_{33}\end{pmatrix},$$

with

$$\begin{aligned}\tilde{A}_{11} &= (B_{12}\nabla\phi_2)\cdot\nabla\phi_2 + (B_{13}\nabla\phi_3)\cdot\nabla\phi_3,\\ \tilde{A}_{22} &= (B_{12}\nabla\phi_1)\cdot\nabla\phi_1 + (B_{23}\nabla\phi_3)\cdot\nabla\phi_3,\\ \tilde{A}_{33} &= (B_{13}\nabla\phi_1)\cdot\nabla\phi_1 + (B_{23}\nabla\phi_2)\cdot\nabla\phi_2.\end{aligned}$$

The reader should note that, when anisotropy is neglected in the interfacial energy – $a(\theta)=1$ in (2) – then the matrix A depends only on $\vec{\phi}$, whereas the matrix $\tilde{A}$ depends only on $\vec{\nabla}\phi$. This property will allow us to prove that the linear system resulting from time and space discretization is stable for any time and space steps, see Appendix A.

We are now in position to write the weak formulation corresponding to (4), plus natural boundary conditions. We are looking for $\vec{\phi}$ and λ such that

$$\begin{aligned}&\frac{1}{M}\left(\frac{\partial\vec{\phi}}{\partial t},\vec{\psi}\right) + (A(\vec{\phi},\nabla\vec{\phi})\nabla\vec{\phi},\nabla\vec{\psi}) + (\tilde{A}(\vec{\phi},\nabla\vec{\phi})\vec{\phi},\vec{\psi}) + (S(c,\vec{\phi}),\vec{\psi}) + (\lambda,\psi_1+\psi_2+\psi_3) = 0,\\ &(\phi_1+\phi_2+\phi_3,\mu) = (1,\mu),\end{aligned} \tag{7}$$

for all test functions $\vec{\psi}$ and μ. Here, $S(c,\vec{\phi})$ denotes the low-order term given by the sum of the Gateaux derivatives of the double well potentials J_{dw} and the phase transformation energy J_{tr}, thus

$$S(c,\vec{\phi}) = \begin{pmatrix}2\left(W_{12}\phi_2^2+W_{13}\phi_3^2\right)\phi_1\\ 2\left(W_{12}\phi_1^2+W_{23}\phi_3^2\right)\phi_2\\ 2\left(W_{13}\phi_1^2+W_{23}\phi_2^2\right)\phi_3 + s(c,T,\phi_3)\end{pmatrix},$$

with

$$s(c,T,\phi_3) = 30\frac{L}{T_{\mathrm{m}}}m_{\mathrm{l}}\left(\frac{c}{\phi_3+k(1-\phi_3)} - \frac{T-T_{\mathrm{m}}}{m_{\mathrm{l}}}\right)\phi_3^2(1-\phi_3)^2.$$

Note that, in order to obtain a formulation similar to those of Nestler and co-workers [20,21,27], we did not take into account the Gateaux derivative of $c/(\phi_3 + k(1-\phi_3))$ with respect to ϕ_3 in the above formulation. Also note that, if the test functions $\vec{\psi}$ and μ belong to the functional spaces $H^1(\Omega)$ and $L^2(\Omega)$, then the above weak formulation makes sense whenever $\vec{\phi}$ and λ belong to $H^1(\Omega) \cap L^\infty(\Omega)$ and $L^2(\Omega)$, for almost all time t.

4. Time and space discretization

For any $h > 0$, consider a finite element mesh of the computational domain Ω into triangles K with size less than h. Let V_h be the usual finite element space of continuous functions, piecewise linear on the triangles of the mesh. Let τ be the time step, $t_n = n\tau$, $n = 0, 1, 2, \ldots$ and let $\vec{\phi}_h^n$, λ_h^n, and c_h^n be finite element approximations of $\vec{\phi}(t_n)$, $\lambda(t_n)$, and $c(t_n)$, respectively. Our numerical method is as follows. At each time step, we first seek for $\vec{\phi}_h^{n+1} = (\phi_{1h}^{n+1}, \phi_{2h}^{n+1}, \phi_{3h}^{n+1})^{\mathrm{T}}$, λ_h^{n+1} in the finite element space V_h such that

$$\begin{aligned}
&\frac{1}{M}\left(\frac{\vec{\phi}_h^{n+1} - \vec{\phi}_h^n}{\tau}, \vec{\psi}_h\right) + \left(A\left(\vec{\phi}_h^n, \nabla\vec{\phi}_h^n\right)\nabla\vec{\phi}_h^{n+1}, \nabla\vec{\psi}_h\right) + \left(\tilde{A}\left(\vec{\phi}_h^n, \nabla\vec{\phi}_h^n\right)\vec{\phi}_h^{n+1}, \vec{\psi}_h\right) \\
&\quad + \left(S\left(c_h^n, \vec{\phi}_h^n\right), \vec{\psi}_h\right) + \left(\lambda_h^{n+1}, \psi_{1h} + \psi_{2h} + \psi_{3h}\right) = 0, \\
&(\phi_{1h} + \phi_{2h} + \phi_{3h}, \mu_h) = (1, \mu_h),
\end{aligned} \tag{8}$$

for all test functions $\vec{\psi} = (\psi_{1h}, \psi_{2h}, \psi_{3h})^{\mathrm{T}}$ and μ_h in V_h. Then, we seek for c_h^{n+1} in the finite element space V_h such that

$$\int_\Omega \frac{c_h^{n+1} - c_h^n}{\tau} d_h + \int_\Omega D(\phi_{3h}^{n+1})\nabla c_h^{n+1}\nabla d_h = \int_\Omega \frac{D(\phi_{3h}^{n+1})(1-k)c_h^n}{\phi_{3h}^{n+1} + k\left(1 - \phi_{3h}^{n+1}\right)}\nabla\phi_{3h}^{n+1} \cdot \nabla d_h, \tag{9}$$

for all test function d_h in the finite element space V_h. The key observation is that in (8) the matrices A and $\tilde{A}$ are evaluated at the previous time step which yields a linear problem. Moreover, it is proved in Appendix A (using the inf–sup framework) that this particular choice yields a linear system which is invertible for all space and time steps h and τ, whenever the anisotropy is neglected in the interfacial energy, that is when $a(\theta) = 1$ in (2). This comforts us about the parabolic nature of the model. Note that all the above integrals are approached using an order two quadrature formula.

Let us write the corresponding algebraic formulation. Let J be the number of vertices of the finite element mesh, the vertices are denoted P_j, $j = 1, \ldots, J$. Let N_j be the continuous functions, piecewise linear on the triangles of the mesh and such that $N_j(P_j) = \delta_{ij}$ (Kronecker symbol). Clearly N_1, N_2, …, N_J is a basis of V_h and we have, for all x in Ω:

$$\begin{aligned}
&\phi_{1h}^n(x) = \sum_{j=1}^J \phi_{1j}^n N_j(x), \quad \phi_{2h}^n(x) = \sum_{j=1}^J \phi_{2j}^n N_j(x), \quad \phi_{3h}^n(x) = \sum_{j=1}^J \phi_{3j}^n N_j(x), \\
&\lambda_h^n(x) = \sum_{j=1}^J \lambda_j^n N_j(x), \quad c_h^n(x) = \sum_{j=1}^J c_j^n N_j(x),
\end{aligned}$$

and define the vectors

$$\vec{\phi}^n = \begin{pmatrix} \vdots \\ \phi^n_{1j} \\ \phi^n_{2j} \\ \phi^n_{3j} \\ \vdots \end{pmatrix}, \quad \vec{\lambda}^n = \begin{pmatrix} \vdots \\ \lambda^n_j \\ \vdots \end{pmatrix}, \quad \vec{c}^n = \begin{pmatrix} \vdots \\ c^n_j \\ \vdots \end{pmatrix}. \tag{10}$$

The algebraic formulation corresponding to (8) and (9) thus consists in seeking $\vec{\phi}^{n+1} \in \mathbb{R}^{3J}$, and $\lambda^{n+1} \in \mathbb{R}^J$ such that

$$\begin{pmatrix} \mathscr{A}^n & \mathscr{B}^{\mathrm{T}} \\ \mathscr{B} & 0 \end{pmatrix} \begin{pmatrix} \vec{\phi}^{n+1} \\ \vec{\lambda}^{n+1} \end{pmatrix} = \begin{pmatrix} \vec{f}^n \\ \vec{g} \end{pmatrix}, \tag{11}$$

then seeking $\vec{c}^{n+1} \in \mathbb{R}^J$ such that

$$\mathscr{D}^n \vec{c}^{n+1} = \vec{\ell}(\phi^{n+1}).$$

Here, the $3J \times 3J$ matrix $\mathscr{A}^n$ corresponds to the time derivative and interfacial energy terms, the $J \times 3J$ matrix $\mathscr{B}$ corresponds to the constraint (1), and the $J \times J$ matrix $\mathscr{D}^n$ to the time derivative and diffusion terms in (5). In Appendix A, we prove that the linear system (11) is uniquely solvable without any restrictions concerning the space and time steps h and τ, using the classical theory of saddle-point problems (see, for instance [28]), provided anisotropy of interfacial energy is neglected. In practice, the above linear system is solved using the GMRES algorithm with a classical ILU algebraic preconditioner.

Following [16,29], we expect that the double well potentials induce a stability condition between the time step and the amplitude of the double wells. Even for the simplest phase-field equation, namely the Allen–Cahn equation $\epsilon u_t = \epsilon \Delta u - (1/\epsilon)(u^3 - u)$, the implicit Euler scheme has a unique solution if $\tau \leqslant \epsilon^2$. The explicit scheme is stable whenever $\tau \leqslant h^2/4$ which is much worse than the previous stability condition if the mesh contains ten or twenty vertices in the direction orthogonal to the interface. Finally, the semi-implicit scheme (diffusion implicit, double well terms explicit) shows the same stability condition as the implicit scheme. Thus, coming back to our finite element formulation, we expect that τ must be smaller than a constant times $1/MW$, where M is the kinetic coefficient of (4) and W is the maximum of W_{12}, W_{13}, and W_{23}. Since these coefficients are related to the width δ of the solid–liquid transition layer (see Section 6 hereafter), in practice τ must be smaller than a constant times δ^2, which does not allow the use of large time steps. However, due to the implicit treatment of all diffusive terms, there is no stability condition between the time step τ and the space step h. Finally, since relatively small time steps are used, the number of iterations required to solve the linear systems is small, always smaller than 50, so that preconditioning is not an issue.

5. Adaptive finite elements with high aspect ratio

Now we propose an adaptive finite element algorithm, the time step τ being fixed. Let N be the number of time steps. The goal of the adaptive algorithm is to build triangulations with high aspect ratio $\mathscr{T}^n_h$, $n = 1, \dots, N$, such that the relative estimated error in the $L^2(0, T; H^1(\Omega))$ norm is close to a preset tolerance TOL. For this purpose, we introduce an error indicator which requires some further notations. This error indicator measures the error in the directions of maximum and minimum stretching of the triangle. The goal of the adaptive algorithm is then to equidistribute the error indicator in the directions of maximum and minimum stretching and to align the directions of maximum and minimum stretching with the directions of maximum and minimum error. We refer to [26] for a theoretical justification in the framework of the heat equation and to [24] for phase field problems.

For any triangle K of the mesh, let $T_K : \hat{K} \to K$ be the affine transformation which maps the reference triangle $\hat{K}$ into K. Let M_K be the Jacobian of T_K that is

$$\mathbf{x} = T_K(\hat{\mathbf{x}}) = M_K \hat{\mathbf{x}} + \mathbf{t}_K.$$

Since M_K is invertible, it admits a singular value decomposition $M_K = R_K^{\mathrm{T}} \Lambda_K P_K$, where R_K and P_K are orthogonal and where Λ_K is diagonal with positive entries. In the following, we set

$$\Lambda_K = \begin{pmatrix} \lambda_{1,K} & 0 \\ 0 & \lambda_{2,K} \end{pmatrix} \quad \text{and} \quad R_K = \begin{pmatrix} \mathbf{r}_{1,K}^{\mathrm{T}} \\ \mathbf{r}_{2,K}^{\mathrm{T}} \end{pmatrix},$$

with the choice $\lambda_{1,K} \geqslant \lambda_{2,K}$. A simple example of such a transformation is $x_1 = H\hat{x}_1, x_2 = h\hat{x}_2$, with $H \geqslant h$, thus

$$M_K = \begin{pmatrix} H & 0 \\ 0 & h \end{pmatrix}, \quad \lambda_{1,K} = H, \quad \lambda_{2,K} = h, \quad \mathbf{r}_{1,K} = \begin{pmatrix} 1 \\ 0 \end{pmatrix}, \quad \mathbf{r}_{2,K} = \begin{pmatrix} 0 \\ 1 \end{pmatrix},$$

see Fig. 3. In other words $\mathbf{r}_{1,K}$ and $\mathbf{r}_{2,K}$ are the directions of maximum and minimum stretching, while $\lambda_{1,K}$ and $\lambda_{2,K}$ measure the amplitude of stretching. Proceeding as in [24,26], we introduce $c_{h\tau}$ the continuous, piecewise linear approximation in time defined by

$$c_{h\tau}(x,t) = \frac{t - t^{n-1}}{\tau} c_h^n(x) + \frac{t^n - t}{\tau} c_h^{n-1}(x), \quad t^{n-1} \leqslant t \leqslant t^n, \ x \in \Omega. \tag{12}$$

Our simplified error indicator is then defined on each time interval $[t^{n-1}, t^n]$ and each triangle K by

$$(\eta_{n,K}(c_{h\tau}))^2 = \int_{t^{n-1}}^{t^n} \frac{1}{2\lambda_{2,K}^{1/2}} \left\| \left[\frac{\partial c_{h\tau}}{\partial n} \right] \right\|_{L^2(\partial K)} \left(\lambda_{1,K}^2 \left(\mathbf{r}_{1,K}^{\mathrm{T}} \tilde{G}_K(c_{h\tau}) \mathbf{r}_{1,K} \right) + \lambda_{2,K}^2 \left(\mathbf{r}_{2,K}^{\mathrm{T}} \tilde{G}_K(c_{h\tau}) \mathbf{r}_{2,K} \right) \right)^{1/2}. \tag{13}$$

Here, $\tilde{G}_K(c_{h\tau})$ is defined by

$$\tilde{G}_K(c_{h\tau}) = \begin{pmatrix} \int_K \left(\eta_1^{ZZ}(c_{h\tau})\right)^2 \mathrm{d}x & \int_K \eta_1^{ZZ}(c_{h\tau}) \eta_2^{ZZ}(c_{h\tau}) \, \mathrm{d}x \\ \int_K \eta_1^{ZZ}(c_{h\tau}) \eta_2^{ZZ}(c_{h\tau}) \, \mathrm{d}x & \int_K \left(\eta_2^{ZZ}(c_{h\tau})\right)^2 \mathrm{d}x \end{pmatrix}, \tag{14}$$

with $\eta_1^{ZZ}(c_{h\tau})$, $\eta_2^{ZZ}(c_{h\tau})$ being the components of the so-called Zienkiewicz–Zhu error estimator

$$\begin{pmatrix} \eta_1^{ZZ}(c_{h\tau}) \\ \eta_2^{ZZ}(c_{h\tau}) \end{pmatrix} = \begin{pmatrix} (I - \Pi_h)\left(\frac{\partial c_{h\tau}}{\partial x_1}\right) \\ (I - \Pi_h)\left(\frac{\partial c_{h\tau}}{\partial x_2}\right) \end{pmatrix}, \tag{15}$$

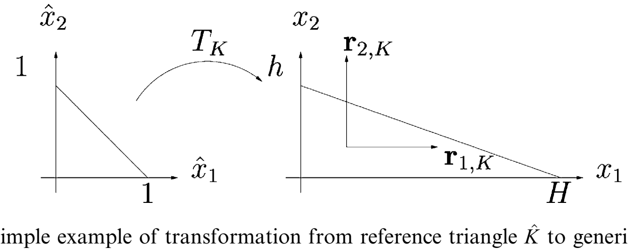

Fig. 3. A simple example of transformation from reference triangle $\hat{K}$ to generic triangle K.

where $\Pi_h(\partial c_{h\tau}/\partial x_1)$ and $\Pi_h(\partial c_{h\tau}/\partial x_2)$ are computed using the formula

$$\begin{pmatrix} \Pi_h\left(\frac{\partial c_{h\tau}}{\partial x_1}\right)(P) \\ \Pi_h\left(\frac{\partial c_{h\tau}}{\partial x_2}\right)(P) \end{pmatrix} = \frac{1}{\sum\limits_{\substack{K\in\mathscr{T}_h\\ P\in K}} |K|} \begin{pmatrix} \sum\limits_{\substack{K\in\mathscr{T}_h\\ P\in K}} |K| \left(\frac{\partial c_{h\tau}}{\partial x_1}\right)_{|K} \\ \sum\limits_{\substack{K\in\mathscr{T}_h\\ P\in K}} |K| \left(\frac{\partial c_{h\tau}}{\partial x_2}\right)_{|K} \end{pmatrix}.$$

The matrix $\tilde{G}_K(c_{h\tau})$ is an estimation of the gradient error in triangle K, therefore, the term $\mathbf{r}_{1,K}^{\mathrm{T}}\tilde{G}_K(c_{h\tau})\mathbf{r}_{1,K}$ in (13) contributes to measuring the error in the direction of the triangle's maximum stretching and the term

$$\int_{t^{n-1}}^{t^n} \frac{1}{2\lambda_{2,K}^{1/2}} \left\| \left[\frac{\partial c_{h\tau}}{\partial n} \right] \right\|_{L^2(\partial K)} \times \lambda_{1,K} \left(\mathbf{r}_{1,K}^{\mathrm{T}} \tilde{G}_K(c_{h\tau}) \mathbf{r}_{1,K} \right)^{1/2}$$

is nothing but the estimated error in the direction of the triangle's maximum stretching.

Our adaptive algorithm aims at building triangulations with high aspect ratio $\mathscr{T}_h^n$, $n = 1, \dots, N$ such that the relative estimated error is close to a preset tolerance TOL, that is:

$$0.75\ \mathrm{TOL} \leqslant \frac{\sum_{n=1}^{N} \sum_{K\in\mathscr{T}_h} (\eta_{n,K}(c_{h\tau}))^2}{\int_0^{\mathrm{T}} \int_\Omega |\nabla c_{h\tau}|^2} \leqslant 1.25\ \mathrm{TOL}. \tag{16}$$

A sufficient condition to satisfy (16) is to build, for each discrete time t_n, $n = 1, \dots, N$, a triangulation with high aspect ratio $\mathscr{T}_h^n$ such that

$$\frac{0.75^2\ \mathrm{TOL}^2}{\mathrm{NV}_h^n} \int_{t^{n-1}}^{t^n} \int_\Omega |\nabla c_{h\tau}|^2 \leqslant (\eta_{n,K}(c_{h\tau}))^2 \leqslant \frac{1.25^2\ \mathrm{TOL}^2}{\mathrm{NV}_h^n} \int_{t^{n-1}}^{t^n} \int_\Omega |\nabla c_{h\tau}|^2$$

for all triangle $K \in \mathscr{T}_h^n$, where NV_h^n is the number of vertices of the mesh $\mathscr{T}_h^n$. We then proceed as in [25,26] to build a mesh having elements with high aspect ratio, using the `BL2D` mesh generator [30]. At each vertex, the estimated error in the directions of maximum and minimum stretching is equidistributed, which yields new desired values of maximum and minimum stretching. Then, the directions of maximum and minimum stretching are aligned with the directions of maximum and minimum error gradient, namely the eigenvectors of the matrix $\tilde{G}_K(c_{h\tau})$.

6. Numerical results

6.1. A one-dimensional test case

In [21], a one-dimensional solidification test case was proposed. Our first task is to reproduce the corresponding results with two-dimensional computations and meshes with elements having high aspect ratio. All the data are given in the MKSA unit system.

The model parameters are those of Rappaz et al. [21], and are the following. The phase field parameters are given by

$$W_{ij} = \frac{3\gamma_{ij}}{\delta}, \quad \epsilon_{ij}^2 = 6\gamma_{ij}\delta, \quad M = \frac{\mu T_{\mathrm{m}}}{6\delta L},$$

Table 1
Parameters used for the simulation

L	T_m	m_l	k	γ_{12}	γ_{13}	γ_{23}	δ	μ	$\dot{T}$	D_s	D_l
10^9	1000	−500	0.5	3.0	1.0	1.0	5×10^{-8}	3×10^{-6}	−10	10^{-13}	10^{-11}

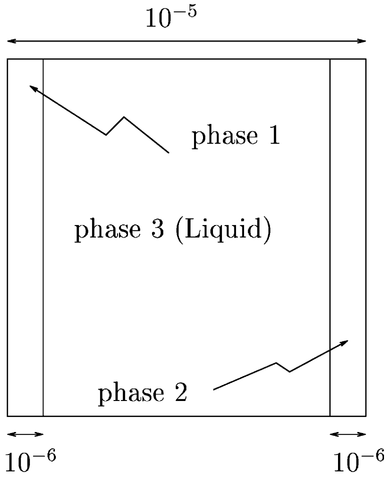

Fig. 4. The one-dimensional test case.

where γ_{13}, γ_{23} denote the boundary energy of grains 1 and 2 (the solid–liquid interfacial energy), γ_{12} is the interfacial energy between grains 1 and 2, δ is the thickness of the solid–liquid interface, and μ a kinetic coefficient.

We consider the computational domain $\Omega = (0; 10^{-5})^2$, an alloy with nominal concentration $c_0 = 4\%$, the model parameters being given in Table 1. The temperature is uniform, equals $T(0) = 980$ °C at initial time and then decreases with constant rate $\dot{T}$. At initial time, solid 1 is present along the left lateral side, solid 2 along the right lateral side, see Fig. 4. Surface tension anisotropy is not considered in this test case, thus $\bar{a} = 0$ in (2). The initial concentrations are those corresponding to the phase diagram, namely $(T(0) - T_m)/m_l$ in the liquid region and $k((T(0) - T_m)/m_l)$ in the solid region. The time step used is $\tau = 0.0005$, the initial mesh is a 1000×2 mesh with about 3000 vertices.

In Figs. 5 and 6, the adapted meshes, concentration and liquid phase profiles are shown when setting TOL $= 0.25$ in (16), that is to say when requiring 25% of relative estimated error. The mesh is refined in the horizontal direction only, close to the phase change region. It can be seen that a thin film of liquid remains entrapped between the two grains during a long time. At time $t = 7$, the liquid phase field ϕ_3 is finally smaller than 1/3 and the boundary can be considered as dry. Refer to [21] for a discussion of coalescence criteria.

Fig. 7 shows the number of vertices generated by the adaptive algorithm as a function of time, with several values of TOL. The CPU time required for these computation from $t = 0$ and 10 (20,000 time steps) on a PC with Pentium III 1.2 GHz is reported in Table 2. Clearly, when TOL is divided by 2, the number of vertices is multiplied by a factor less than 4, and so is the CPU time. It should be noted that the aspect ratio of the triangles can reach values larger than 6000!

In Fig. 8, some results are reported when keeping TOL unchanged, but varying the width δ of the solid–liquid region. Each time δ is divided by 2, the time step should be divided by 4, for stability reasons detailed in Section 4. It can be seen that the CPU time is multiplied by a factor less than eight each time δ is divided by 2. This is a favorable situation since a two-dimensional explicit method without adaptive refinement requires, due to the Fourier stability condition, the CPU time to be multiplied by 16 each time δ is divided by 2.

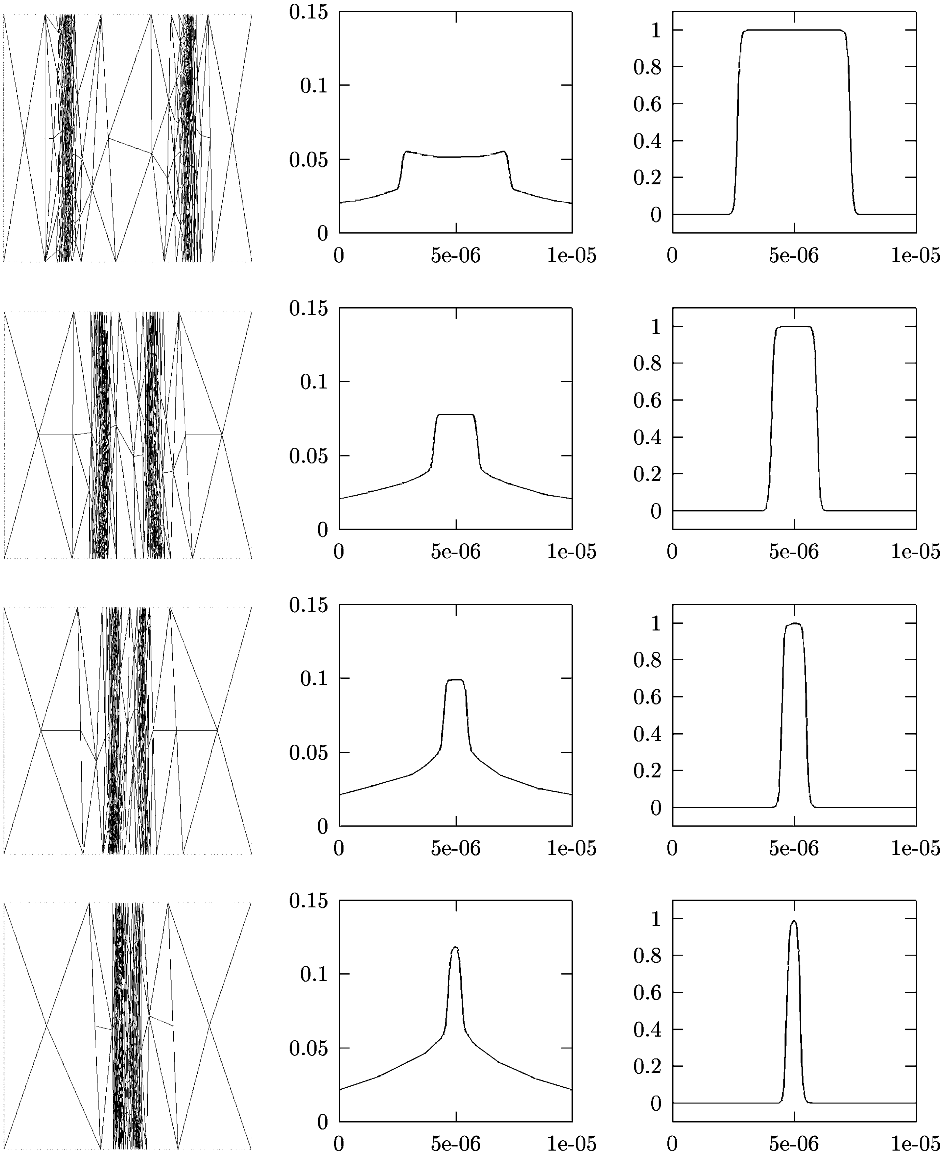

Fig. 5. The one-dimensional test case. Numerical results with TOL = 0.25. Adapted meshes (left column), concentration profile (middle column), and liquid phase field profile (right column) from time $t = 1$ (first row, temperature $T = 970$ °C) until time $t = 4$ (last row, temperature $T = 940$ °C).

6.2. A two-dimensional test case

Now we consider a two-dimensional test case in order to illustrate the possibilities of our numerical model. At initial time, four circular solid seeds of diameter 4×10^{-7} are placed in the computational domain $\Omega = (0; 3 \times 10^{-5})^2$. The two lower (resp., upper) solid seeds correspond to solid 1 (resp., solid 2). For instance these two seeds could correspond to two arms of the same three-dimensional dendrite. The an-

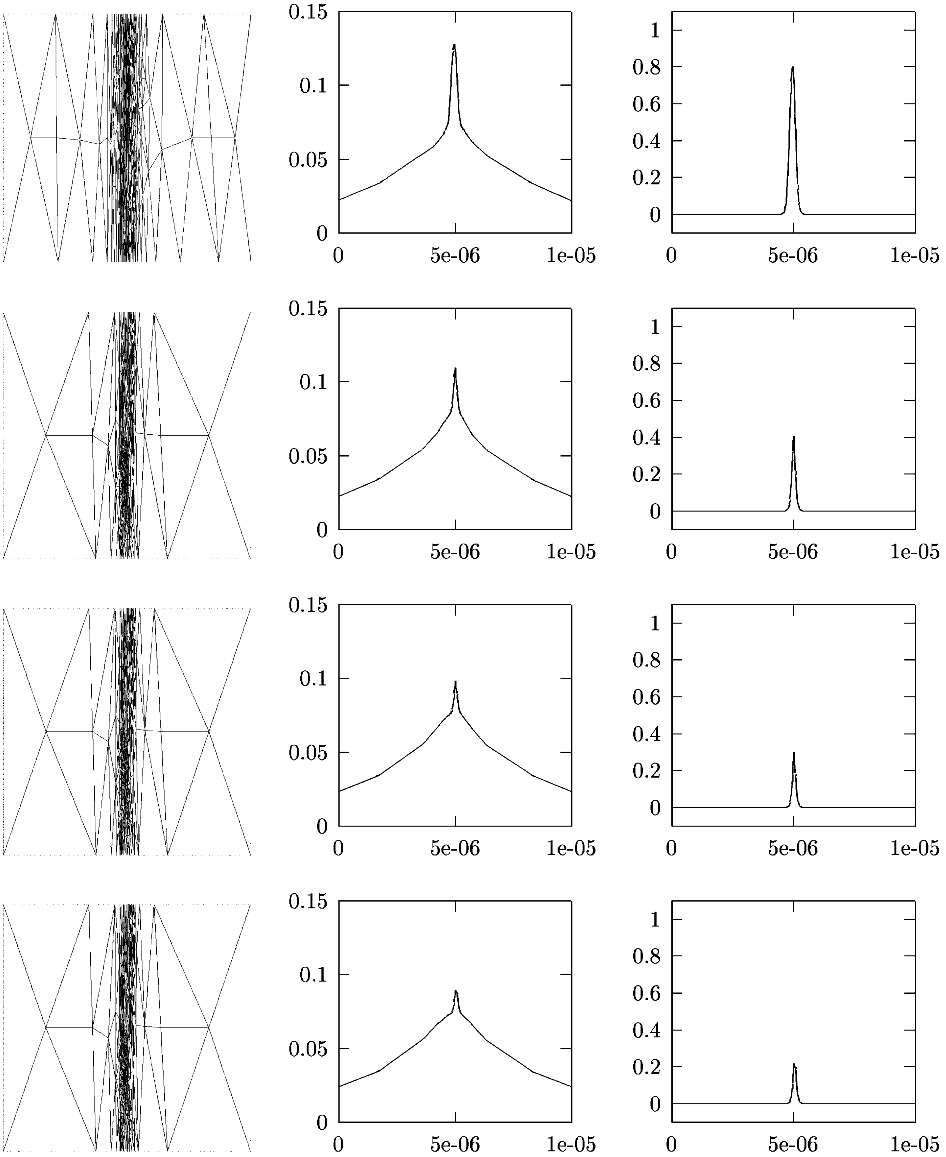

Fig. 6. The one-dimensional test case. Numerical results with TOL = 0.25. Adapted meshes (left column), concentration profile (middle column) and liquid phase field profile (right column) from time $t = 5$ (first row, temperature $T = 930$ °C) until time $t = 8$ (last row, temperature $T = 900$ °C).

isotropic coefficient is $\bar{a} = 0.04$, the angles defined in (3) are $\theta^0_{12} = \pi/8$, $\theta^0_{13} = 0$, $\theta^0_{23} = \pi/4$. The temperature is uniform, equals 900 °C at initial time and then decreases with constant rate $\dot{T}$. The physical parameters are now those of Table 3. The values of the parameters are physical and are taken from [21], except the width of the interface δ which is 5×10^{-8}, the physical value being 1–5 nm. In [21], two-dimensional computations have been performed with physical values, but with a simpler geometry. Indeed, the boundary conditions were periodic so that the interface at the end of the simulation was along the boundaries of the computational domain. Explicit finite volume techniques were used and the mesh was

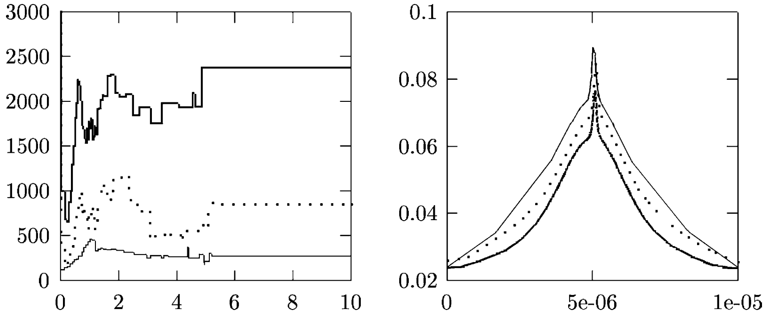

Fig. 7. The one-dimensional test case. Numerical results with TOL = 0.25 (thin line), 0.125 (dotted line), and 0.0625 (bold line). Left: number of vertices of the adapted meshes with elements having high aspect ratio, with respect to time. Right: concentration profile at time $t = 8$.

Table 2
The one-dimensional test case

TOL	# Vertices	# Meshes	CPU
0.25	272	49	4809
0.125	849	57	14,734
0.0625	2379	47	46,425

Number of vertices of the final mesh, number of generated meshes and CPU time in seconds with respect to TOL.

δ	#TimeSteps	#Vertices	#Meshes	CPU
$5\ 10^{-8}$	20000	272	49	4809
$2.5\ 10^{-8}$	80000	1508	268	36861
$1.25\ 10^{-8}$	320000	659	676	249096

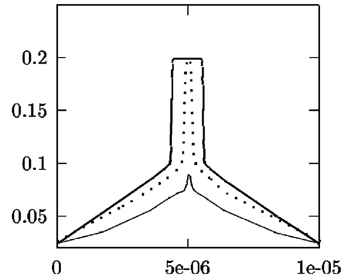

Fig. 8. The one-dimensional test case. Numerical results with TOL = 0.25 and several values of δ. Top: number of time steps from $t = 0$ to 10, number of vertices of the final mesh, number of generated meshes and CPU time in seconds with respect to δ. Bottom: concentration profile at time $t = 8$, $\delta = 5 \times 10^{-8}$ (thin line), $\delta = 2.5 \times 10^{-8}$ (dotted line), and $\delta = 1.25 \times 10^{-8}$ (bold line).

Table 3
Parameters used for the simulation

L	T_m	m_l	k	γ_{12}	γ_{13}	γ_{23}	δ	μ	$\dot{T}$	D_s	D_l
10^9	1000	−500	0.5	3.0	1.0	1.0	5×10^{-8}	3×10^{-6}	−40	10^{-10}	10^{-10}

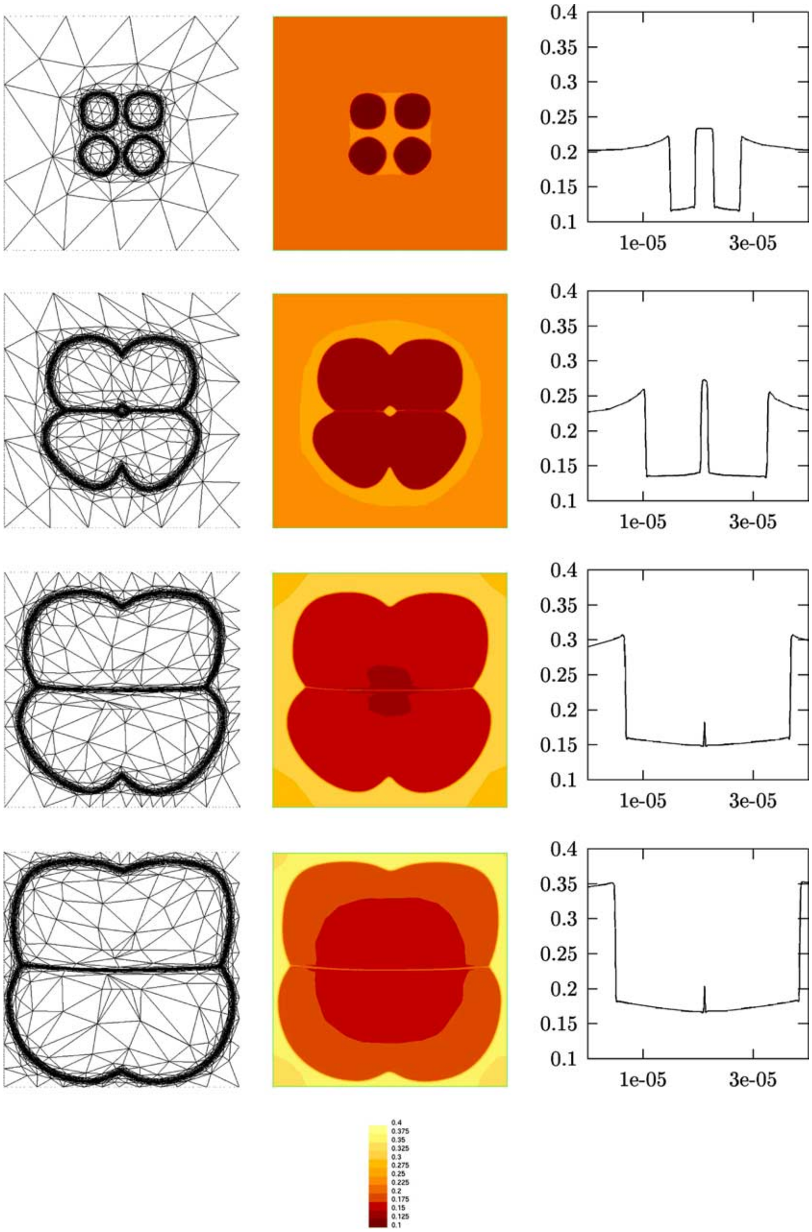

Fig. 9. The two-dimensional test case. The two lower (resp., upper) seeds have phase index 1 (resp., 2). Numerical results with TOL = 0.25. Adapted meshes (left column), concentration field (middle column), and profile along first diagonal (right column) from time $t = 0.5$ (first row) until time $t = 2$ (last row).

refined along the boundaries of the computational domain. At initial time, δ was chosen to be large, $\delta = 10^{-8}$, then at the end of the simulation, as the interface was close to the boundaries of the computational domain, δ was reduced to $\delta = 10^{-9}$. The required CPU time was of the order of a week so that no realistic two-dimensional computations were possible.

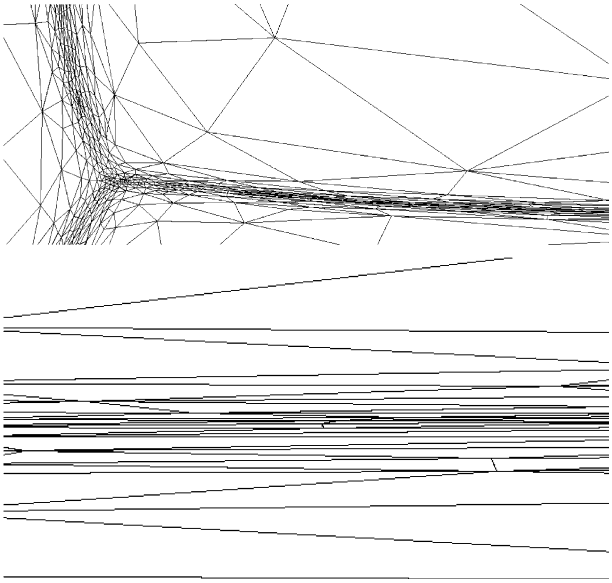

Fig. 10. The two-dimensional test case. Numerical results with TOL $= 0.25$. Zooms of the adapted mesh at time $t = 2$.

In Fig. 9, the results corresponding to a computation with time step $\tau = 0.001$ and tolerance TOL $= 0.25$ are shown. Clearly, the two solid regions having the same phase index (1 for the lower regions and 2 for the upper ones) merge easily. However, the two resulting grains do not merge due to the interfacial energy between solid 1 and solid 2. As a consequence, a thin layer of liquid of high concentration remains between the two grains. Zooms of the final adapted mesh are reported in Fig. 10. Clearly, the mesh aspect ratio is very large in phase change regions with large radius of curvature, whereas isotropic triangles are obtained in phase change regions with small radius of curvature. In order to show the potential of our adaptive algorithm, a computation corresponding to the case when the solid seeds are initially distributed along the diagonals has been performed. The results are reported in Fig. 11 and are significantly different from those of Fig. 9, showing that several coalescence patterns can be obtained. The asymmetric pattern obtained with this calculation is due to the anisotropy of the surface energy. The solid regions 2, which are located on the second diagonal, have preferred growth directions parallel to the diagonals ($\theta_{23}^0 = \pi/4$), whereas solid regions 1 have their preferred growth directions aligned with the horizontal and vertical axes ($\theta_{13}^0 = 0$). Since the surface energy is maximum along the preferred growth directions, it is energetically more favorable to bridge solid 1 than solid 2.

7. Conclusions and perspectives

A multiphase-field model for the description of coalescence of dendritic grains in a binary alloy has been implemented numerically using adaptive finite elements with high aspect ratio. At each time step two linear systems are solved, one for the solute concentration, the other for the phase fields and a Lagrange multiplier. The implicit treatment of diffusion terms allows the Fourier stability condition to be avoided. The meshes contain elements having high aspect ratio and are generated automatically during the computation using a criteria based on an appropriate error indicator.

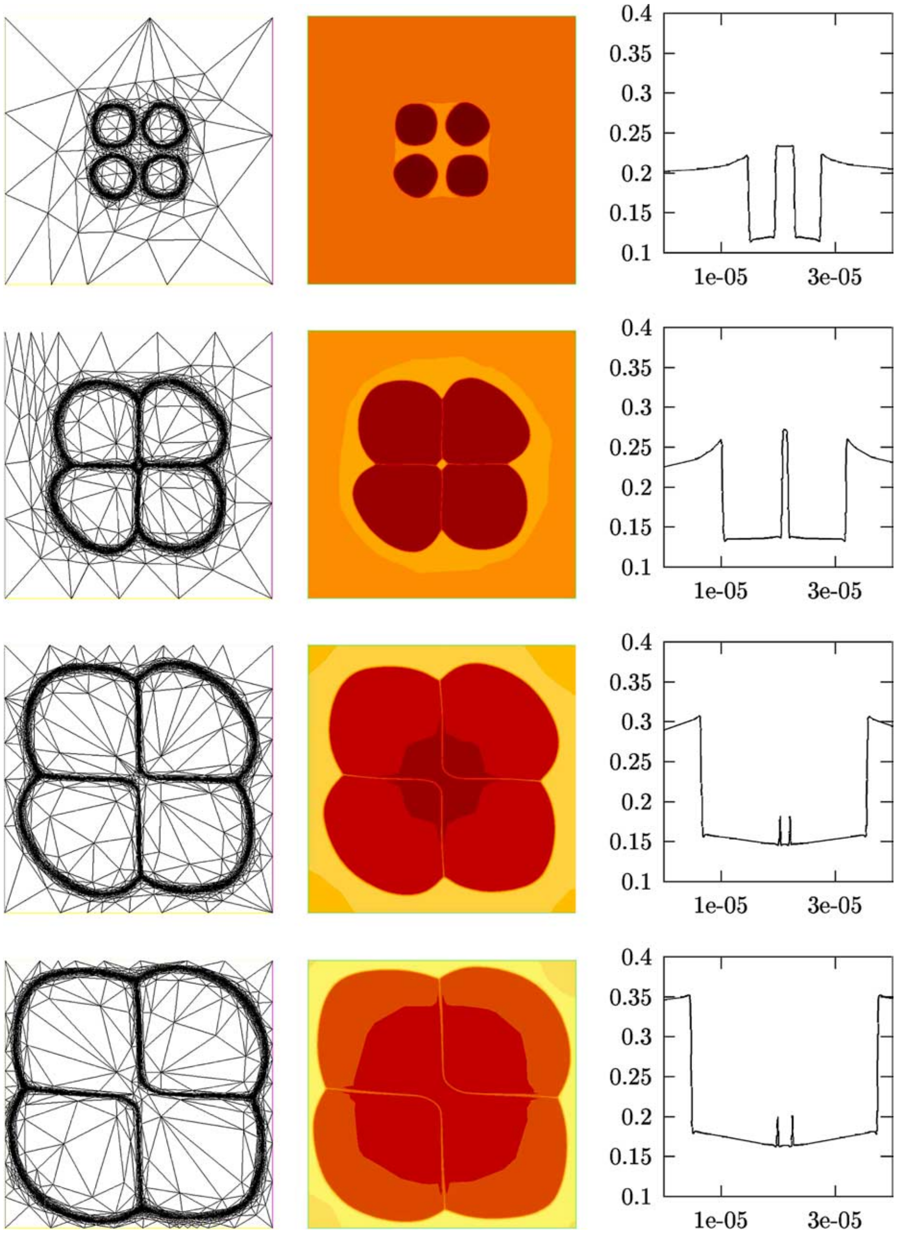

Fig. 11. The two-dimensional test case. The two seeds along the first (resp., second) diagonal have phase index 1 (resp., 2). Numerical results with TOL $= 0.25$. Adapted meshes (left column), concentration field (middle column) and profile along first diagonal (right column) from time $t = 0.5$ (first row) until time $t = 2$ (last row).

The results obtained for one and two-dimensional problems show the efficiency of the method. The use of meshes with elements having high aspect ratio allows accurate computations to be performed with fewer vertices than isotropic finite elements or regular grids. This approach is particularly interesting for problems where the interface thickness is very small compared to the size of the computational domain. Each time the interface thickness is divided by 2, the spatial resolution in the vicinity of the interface has to be increased by a factor 2 to keep the same accuracy. In methods based on regular grids and explicit formulations, this corresponds to multiply the CPU time by 16. It was shown that with the present method this factor is less than 8, even though there is an additional cost due to the resolution of the linear systems and the remeshing procedure. Therefore, adaptive finite elements with high aspect ratio should be more efficient than methods based on regular grids and explicit formulations when the interface thickness is small.

Appendix A. Proof that the linear system (11) is uniquely solvable

From a mathematical standpoint, existence of a solution to the multiphase-field problem (4) and (5) remains an open problem. In this section, we aim to give some preliminary results in the isotropic case, that is when $\bar{a} = 0$ in (2), and when $\epsilon_{12} = \epsilon_{13} = \epsilon_{23} = 1$.

We consider the weak formulation (7) and state the following formal coercivity property.

Lemma A.1. *For all function* $\vec{\psi} = (\psi_1, \psi_2, \psi_3)^{\mathrm{T}}$ *such that* $\psi_1 + \psi_2 + \psi_3 = 1$, *we have*

$$\int_\Omega |\nabla\vec{\psi}|^2 \leqslant 4((A(\vec{\psi})\nabla\vec{\psi}, \nabla\vec{\psi}) + (\tilde{A}(\nabla\vec{\psi})\vec{\psi}, \vec{\psi})).$$

Proof. Let $\mathbf{r}(\cdot,\cdot)$ be defined by $\mathbf{r}(\psi_i, \psi_j) = \psi_i\nabla\psi_j - \psi_j\nabla\psi_i$. Using the fact that $\psi_1 + \psi_2 + \psi_3 = 1$, a simple calculation yields

$$\nabla\psi_j = -\sum_{k=1}^{3} \mathbf{r}(\psi_j, \psi_k), \quad j = 1, 2, 3.$$

Then, we have

$$\int_\Omega |\nabla\vec{\psi}|^2 = \int_\Omega \sum_{j=1}^{3} |\nabla\psi_j|^2 = \int_\Omega \sum_{j=1}^{3} \left| \sum_{k=1}^{3} \mathbf{r}(\psi_j, \psi_k) \right|^2 \leqslant 4 \int_\Omega \sum_{j=1}^{3} \sum_{k>j} |\mathbf{r}(\psi_j, \psi_k)|^2.$$

On the other hand, from the calculations of Section 3, we have

$$(A(\vec{\psi})\nabla\vec{\psi}, \nabla\vec{\psi}) + (\tilde{A}(\nabla\vec{\psi})\vec{\psi}, \vec{\psi}) = \int_\Omega \sum_{j=1}^{3} \sum_{k>j} |\mathbf{r}(\psi_j, \psi_k)|^2,$$

which completes the proof. □

Now we provide some information about the matrices A and $\tilde{A}$ defined in Section 3.

Lemma A.2. *Let* I *be the* 2×2 *unit matrix. For all* $\vec{\xi} = (\xi_1, \xi_2, \xi_3)^{\mathrm{T}} \in \mathbb{R}^3$ *and for all* $\vec{\zeta} = (\zeta_1, \zeta_2, \zeta_3, \zeta_4, \zeta_5, \zeta_6)^{\mathrm{T}} \in \mathbb{R}^6$, *the matrices* $A(\vec{\xi})$ *and* $\tilde{A}(\vec{\zeta})$ *defined by*

$$A(\vec{\xi}) = \begin{pmatrix} (\xi_2^2 + \xi_3^2)I & -\xi_1\xi_2 I & -\xi_1\xi_3 I \\ -\xi_1\xi_2 I & (\xi_1^2 + \xi_3^2)I & -\xi_2\xi_3 I \\ -\xi_1\xi_3 I & -\xi_2\xi_3 I & (\xi_1^2 + \xi_2^2)I \end{pmatrix}$$

and

$$\tilde{A}(\vec{\zeta}) = \begin{pmatrix} \zeta_3^2 + \zeta_4^2 + \zeta_5^2 + \zeta_6^2 & -(\zeta_1\zeta_3 + \zeta_2\zeta_4) & -(\zeta_1\zeta_5 + \zeta_2\zeta_6) \\ -(\zeta_1\zeta_3 + \zeta_2\zeta_4) & \zeta_1^2 + \zeta_2^2 + \zeta_5^2 + \zeta_6^2 & -(\zeta_3\zeta_5 + \zeta_4\zeta_6) \\ -(\zeta_1\zeta_5 + \zeta_2\zeta_6) & -(\zeta_3\zeta_5 + \zeta_4\zeta_6) & \zeta_1^2 + \zeta_2^2 + \zeta_3^2 + \zeta_4^2 \end{pmatrix}$$

are symmetric positive semi-definite. Moreover, the matrix $A(\vec{\xi})$ *has eigenvalues* $\lambda_i(\vec{\xi})$ *and orthonormal eigenvectors* $\mathbf{R}_i(\vec{\xi})$ *given by*

$$\lambda_1(\vec{\xi}) = \lambda_2(\vec{\xi}) = \lambda_3(\vec{\xi}) = \lambda_4(\vec{\xi}) = \xi_1^2 + \xi_2^2 + \xi_3^2, \quad \lambda_5(\vec{\xi}) = \lambda_6(\vec{\xi}) = 0,$$

and

$$\begin{aligned} &\mathbf{R}_1(\vec{\xi}) = r_1(0,0,0,-\xi_3,0,\xi_2)^{\mathrm{T}}, \quad \mathbf{R}_2(\vec{\xi}) = r_2\big(0,-\big(\xi_2^2+\xi_3^2\big),0,\xi_1\xi_2,0,\xi_1\xi_3\big), \\ &\mathbf{R}_3(\vec{\xi}) = r_1(0,0,-\xi_3,0,\xi_2,0)^{\mathrm{T}}, \quad \mathbf{R}_4(\vec{\xi}) = r_2\big(-\big(\xi_2^2+\xi_3^2\big),0,\xi_1\xi_2,0,\xi_1\xi_3,0\big)^{\mathrm{T}}, \\ &\mathbf{R}_5(\vec{\xi}) = r_3(0,\xi_1,0,\xi_2,0,\xi_3)^{\mathrm{T}}, \quad \mathbf{R}_6(\vec{\xi}) = r_3(\xi_1,0,\xi_2,0,\xi_3,0)^{\mathrm{T}}, \end{aligned}$$

where normalization factors r_i, $i = 1, 2, 3$ *are given by*

$$r_1 = \frac{1}{\sqrt{\xi_2^2+\xi_3^2}}, \quad r_2 = \frac{1}{\sqrt{\big(\xi_2^2+\xi_3^2\big)^2 + \xi_1^2\xi_2^2 + \xi_1^2\xi_3^2}}, \quad r_3 = \frac{1}{\sqrt{\xi_1^2+\xi_2^2+\xi_3^2}}.$$

Proof. The fact that the matrices are positive semi-definite is a consequence of Young's inequality ($2ab \leqslant a^2 + b^2$, $a, b \in \mathbb{R}$). The eigenvalues and eigenvectors of $A(\vec{\xi})$ can be obtained using the Maple software, for instance. □

Remark 1. The fact that the matrices $A(\vec{\phi})$ and $\tilde{A}(\nabla\vec{\phi})$ are symmetric positive semi-definite implies that the interfacial energy contribution J_{int} defined in Section 2 is convex with respect to $\nabla\vec{\phi}$ and $\vec{\phi}$, respectively.

In order to prove that the linear system (11) is uniquely solvable, we need the following technical result.

Lemma A.3. *Let* $\vec{\xi} = (\xi_1, \xi_2, \xi_3)^{\mathrm{T}} \in \mathbf{R}^3$ *such that* $\xi_1 + \xi_2 + \xi_3 = 1$. *Then, there exists* $C > 0$ (*depending on* $|\vec{\xi}|$) *such that, for all* $\vec{x} = (x_1, x_2, x_3, x_4, x_5, x_6) \in \mathbb{R}^6$ *with* $x_1 + x_3 + x_5 = 0$ *and* $x_2 + x_4 + x_6 = 0$, *we have*

$$\vec{x}^{\mathrm{T}} A(\vec{\xi})\vec{x} \geqslant C\vec{x}^{\mathrm{T}}\vec{x}.$$

Proof. Let $\vec{\xi} = (\xi_1, \xi_2, \xi_3)^{\mathrm{T}} \in \mathbf{R}^3$ such that $\xi_1 + \xi_2 + \xi_3 = 1$. Let $\vec{x} = (x_1, x_2, x_3, x_4, x_5, x_6) \in \mathbb{R}^6$ such that $x_1 + x_3 + x_5 = 0$ and $x_2 + x_4 + x_6 = 0$. We can write $\vec{x}$ in the basis of the eigenvectors $\mathbf{R}_i(\vec{\xi})$ of the matrix $A(\vec{\xi})$:

$$\vec{x} = \sum_{i=1}^{6} \alpha_i(\vec{\xi})\mathbf{R}_i(\vec{\xi}). \tag{A.1}$$

Since the eigenvectors $\mathbf{R}_i$ are orthonormal and since eigenvalues λ_5 and λ_6 are zero, we obtain, using the previous lemma:

$$\vec{x}^{\mathrm{T}} A(\vec{\xi})\vec{x} = \sum_{i=1}^{4} (\alpha_i(\vec{\xi}))^2 \lambda_i(\vec{\xi}) = \sum_{i=1}^{4} (\alpha_i(\vec{\xi}))^2 \big(\xi_1^2 + \xi_2^2 + \xi_3^2\big).$$

Since $\xi_1 + \xi_2 + \xi_3 = 1$, we have, using Young's inequality $\xi_1^2 + \xi_2^2 + \xi_3^2 \geqslant \frac{1}{2}$, so that

$$\vec{x}^{\mathrm{T}}A(\vec{\xi})\vec{x} \geqslant \frac{1}{2}\sum_{i=1}^{4}(\alpha_i(\vec{\xi}))^2.$$

Thus, if we could prove that there exists $C > 0$ (depending on $\vec{\xi}$) such that

$$(\alpha_5(\vec{\xi}))^2 + (\alpha_6(\vec{\xi}))^2 \leqslant C\sum_{i=1}^{4}(\alpha_i(\vec{\xi}))^2, \tag{A.2}$$

we would obtain

$$\vec{x}^{\mathrm{T}}A(\vec{\xi})\vec{x} \geqslant \frac{1}{2(1+C)}\sum_{i=1}^{6}(\alpha_i(\vec{\xi}))^2 = \frac{1}{2(1+C)}\vec{x}^{\mathrm{T}}\vec{x},$$

and the result would be proved. It thus remain to prove (A.2). For this purpose, we write components 1, 3, and 5 of (A.1) to obtain:

$$\begin{aligned}
x_1 &= -\alpha_4 r_2\left(\xi_2^2 + \xi_3^2\right) + \alpha_6 r_3 \xi_1,\\
x_3 &= -\alpha_3 r_1 \xi_3 + \alpha_4 r_2 \xi_1 \xi_2 + \alpha_6 r_3 \xi_2,\\
x_5 &= \alpha_3 r_1 \xi_2 + \alpha_4 r_2 \xi_1 \xi_3 + \alpha_6 r_3 \xi_3.
\end{aligned}$$

Summing these three equations, taking into account the fact that $\xi_1 + \xi_2 + \xi_3 = 1$ and $x_1 + x_3 + x_5 = 0$ yields

$$\alpha_6 = \sqrt{\xi_1^2 + \xi_2^2 + \xi_3^2}\left(\alpha_4 \frac{\xi_2^2 + \xi_3^2 - \xi_1\xi_2 - \xi_1\xi_3}{\sqrt{\left(\xi_2^2 + \xi_3^2\right)^2 + \xi_1^2\xi_2^2 + \xi_1^2\xi_3^2}} + \alpha_3 \frac{\xi_3 - \xi_2}{\sqrt{\xi_2^2 + \xi_3^2}}\right),$$

which yields $|\alpha_6| \leqslant C(|\vec{\xi}|)(|\alpha_3| + |\alpha_4|)$. We then write components 2, 4, and 6 of (A.1) and obtain $|\alpha_5| \leqslant C(|\vec{\xi}|)(|\alpha_1| + |\alpha_2|)$, which completes the proof. □

We are now in position to prove that the linear system (11) is uniquely solvable. For this purpose, the finite element scheme (8) is rewritten in the following abstract form:

$$\begin{aligned}
&a\left(\vec{\phi}_h^n\right)\left(\vec{\phi}_h^{n+1}, \vec{\psi}_h\right) + b\left(\lambda_h^{n+1}, \vec{\psi}_h\right) = f^n(\vec{\psi}_h),\\
&b\left(\mu_h, \vec{\phi}_h^{n+1}\right) = (1, \mu_h),
\end{aligned} \tag{A.3}$$

where the bilinear forms $a(\vec{\phi}_h^n)$ and b are defined for all $\vec{\phi}_h = (\phi_{1h}, \phi_{2h}, \phi_{3h})^{\mathrm{T}}$, $\vec{\psi}_h = (\psi_{1h}, \psi_{2h}, \psi_{3h})^{\mathrm{T}}$ and λ_h in the finite element space by

$$\begin{aligned}
&a\left(\vec{\phi}_h^n\right)\left(\vec{\phi}_h, \vec{\psi}_h\right) = \frac{1}{\tau}(\vec{\phi}_h, \vec{\psi}_h) + \left(A\left(\vec{\phi}_h^n\right)\nabla\vec{\phi}_h, \nabla\vec{\psi}_h\right) + \left(\tilde{A}\left(\nabla\vec{\phi}_h^n\right)\vec{\phi}_h, \vec{\psi}_h\right),\\
&b(\lambda_h, \vec{\psi}_h) = (\lambda_h, \psi_{1h} + \psi_{2h} + \psi_{3h}).
\end{aligned}$$

We then have the following result.

Lemma A.4. *Assume that* $\vec{\phi}_h^n = (\phi_{1h}^n, \phi_{2h}^n, \phi_{2h}^n)^{\mathrm{T}}$ *is in the finite element space with* $\phi_{1h}^n + \phi_{2h}^n + \phi_{2h}^n = 1$. *Then, the finite element scheme* (A.3) *and therefore the linear system* (11) *are uniquely solvable.*

Proof. Let $V = H^1(\Omega)$, let V_h the finite element space of continuous, piecewise linear functions. The goal is to use Brezzi's inf–sup framework, see [28], for instance. Let $\vec{\phi}_h^n = (\phi_{1h}^n, \phi_{2h}^n, \phi_{2h}^n)^{\mathrm{T}} \in V_h^3$ be the solution at previous time with $\phi_{1h}^n + \phi_{2h}^n + \phi_{2h}^n = 1$. We are going to prove that the bilinear forms $a(\vec{\phi}_h^n) : V^3 \times V^3 \to \mathbb{R}$ and $b : V' \times V^3 \to \mathbb{R}$ satisfy the following conditions:

(i) There exists $C > 0$ (depending on $\vec{\phi}_h^n$) such that for all $h, \tau > 0$, for all $\vec{\psi}_h = (\psi_{1h}, \psi_{2h}, \psi_{3h})^{\mathrm{T}} \in V_h^3$ such that $\psi_{1h} + \psi_{2h} + \psi_{3h} = 0$, we have:

$$a\left(\vec{\phi}_h^n\right)(\vec{\psi}_h, \vec{\psi}_h) \geqslant C\|\vec{\psi}_h\|_V^2.$$

(ii) Let $\mu_h \in V_h$, we have:

$$\text{If } b(\mu_h, \vec{\psi}_h) = 0 \quad \text{for all } \vec{\psi}_h = (\psi_{1h}, \psi_{2h}, \psi_{3h})^{\mathrm{T}} \in V_h^3, \quad \text{then } \mu_h = 0. \tag{A.4}$$

Note that condition (i) is equivalent to the fact that the matrix A^n of (11) is coercive on the kernel of B, whereas condition (ii) corresponds to $\mathrm{Ker}(B^{\mathrm{T}}) = 0$.

Proving condition (ii) is a trivial task. Indeed, choosing $\vec{\psi}_h = (\mu_h, 0, 0)^{\mathrm{T}}$ in (A.4) yields the result. To prove condition (i), we consider a function $\vec{\psi}_h = (\psi_{1h}, \psi_{2h}, \psi_{3h})^{\mathrm{T}} \in V_h^3$ such that $\psi_{1h} + \psi_{2h} + \psi_{3h} = 0$. Thus, $\nabla\psi_{1h} + \nabla\psi_{2h} + \nabla\psi_{3h} = 0$ and we can use Lemma A.3 to obtain

$$a\left(\vec{\phi}_h^n\right)(\vec{\psi}_h, \vec{\psi}_h) \geqslant \int_\Omega A\left(\vec{\phi}_h^n\right)\nabla\vec{\psi}_h \cdot \nabla\vec{\psi}_h \geqslant C\int_\Omega |\nabla\vec{\psi}_h|^2,$$

where C depends on $\vec{\phi}_h^n$. □

Remark 2. In the case when ϕ_{1h}^n, ϕ_{2h}^n, and $\phi_{3h}^n \in [0, 1]$, the constant C in (i) is bounded from below, so that our discretization procedure inherits the coercivity property of Lemma A.1.

References

[1] D. Stefanescu, J. Warren, M. Jolly, M. Krane, Modeling of Casting, Welding, and Advanced Solidification Processes X, The Minerals, Metals and Materials Society, Warrendale, PA, 2003.

[2] A. Jacot, M. Rappaz, A pseudo front tracking technique for the modelling of solidification microstructures in multicomponent alloys, Acta Mater. 50 (2002) 1909–1926.

[3] D. Juric, G. Tryggvason, A front-tracking method for dendritic solidification, J. Comput. Phys. 123 (1996) 127–148.

[4] G. Caginalp, J.-T. Lin, A numerical analysis of an anisotropic phase field model, IMA J. Appl. Math. 39 (1) (1987) 51–66.

[5] G. Caginalp, E.A. Socolovsky, Efficient computation of a sharp interface by spreading via phase field methods, Appl. Math. Lett. 2 (2) (1989) 117–120.

[6] G. Caginalp, W. Xie, Phase-field and sharp-interface alloy models, Phys. Rev. E 48 (3) (1993) 1897–1909.

[7] G. Caginalp, X. Chen, Convergence of the phase field model to its sharp interface limits, Eur. J. Appl. Math. 9 (4) (1998) 417–445.

[8] A. Fasano, M. Primicerio (Eds.), Free Boundary Problems: Theory and Applications, Research Notes in Mathematics, vols. I, II, and 78, Pitman Advanced Publishing Program, Boston, MA, 1983.

[9] J. Langer, Models of pattern formation in first-order phase transitions, in: Directions in Condensed Matter Physics, Series on Directions in Condensed Matter Physics, vol. 1, World Scientific, Singapore, 1986.

[10] J. Collins, H. Levine, Diffuse interface model of diffusion-limited crystal growth, Phys. Rev. B 31 (9) (1985) 6119–6122.

[11] R. Kobayashi, Modeling and numerical simulations of dendritic crystal growth, Physica D 63 (1993) 410–423.

[12] A. Karma, Phase-field model of eutectic growth, Phys. Rev. E 49 (1994) 2245–2250.

[13] J. Warren, W. Boettinger, Prediction of dendritic growth and microseggregation patterns in a binary alloy using the phase-field model, Acta Metall. Mater. 43 (2) (1995) 689–703.

[14] W. Boettinger, J. Warren, C. Beckermann, A. Karma, Phase-field simulation of solidification, Annual Rev. Mater. Res. 32 (2002) 163–194.

[15] L. Chen, Phase-field models for microstructure evolutions, Annual Rev. Mater. Res. 32 (2002) 163–194.

[16] C.M. Elliott, Approximation of curvature dependent interface motion, in: The State of the Art in Numerical Analysis (York, 1996), Oxford University Press, New York, 1997, pp. 407–440.

[17] A. Visintin, Models of Phase Transitions, Birkhäuser Boston Inc., Boston, MA, 1996.

[18] A. Wheeler, G. McFadden, W. Boettinger, Phase-field model for solidification of a eutectic alloy, Proc. Roy. Soc. Lond. Ser. A Math. Phys. Engrg. Sci. 452 (1946) (1996) 495–525.

[19] J. Tiaden, B. Nestler, H. Diepers, I. Steinbach, The multiphase-field model with an integrated concept for modelling solute diffusion, Physica D: Nonlinear Phenomena 115 (1–2) (1998) 73–86.

[20] B. Nestler, A. Wheeler, A multiphase-field model of eutectic and peritectic alloys: numerical simulation of growth structures, Physica D 138 (1–2) (2000) 114–133.

[21] M. Rappaz, A. Jacot, W. Boettinger, Last stage solidification of alloys: a theoretical study of dendrite arm and grain coalescence, Met. Trans. A 34 (2003) 467–479.

[22] N. Provatas, N. Goldenfeld, J. Dantzig, Adaptive mesh refinement computation of solidification microstructures using dynamic data structures, J. Comput. Phys. 148 (1) (1999) 265–290.

[23] A. Schmidt, Computation of three dimensional dendrites with finite elements, J. Comput. Phys. 125 (2) (1996) 293–312.

[24] E. Burman, M. Picasso, Anisotropic, adaptive finite elements for the computation of a solutal dendrite, J. Interface Free Boundaries 5 (2003) 103–127.

[25] M. Picasso, Numerical study of the effectivity index for an anisotropic error indicator based on Zienkiewicz–Zhu error estimator, Comm. Numer. Methods Engrg. 19 (2002) 13–23.

[26] M. Picasso, An anisotropic error indicator based on Zienkiewicz–Zhu error estimator: application to elliptic and parabolic problems, SIAM J. Sci. Comput. 24 (2003) 1328–1355.

[27] H. Garcke, B. Nestler, B. Stoth, A multiphase-field concept: numerical simulations of moving phase boundaries and multiple junctions, SIAM J. Appl. Math. 60 (1) (2000) 295–315 (electronic).

[28] F. Brezzi, K. Bathe, A discourse on the stability conditions for mixed finite element formulations, Comput. Methods Appl. Mech. Engrg. 82 (1–3) (1990) 27–57 (reliability in computational mechanics (Austin, TX, 1989)).

[29] C. Elliott, A. Stuart, The global dynamics of discrete semilinear parabolic equations, SIAM J. Numer. Anal. 30 (6) (1993) 1622–1663.

[30] H. Borouchaki, P. Laug, The BL2D mesh generator: beginner's guide, user's and programmer's manual, Technical Report RT-0194, Institut National de Recherche en Informatique et Automatique (INRIA), Rocquencourt, 78153 Le Chesnay, France, 1996.